Journal Name

ARTICLE

Multigrain Electrospun Nickel Doped Lithium Titanate Nanofibers with High Power Lithium Ion Storage

Salah Abureden, Fathy M Hassan, Gregory Lui, Wook Ahn, Serubbabel Sy, Aiping Yu, and Zhongwei Chen †

A novel in-situ nickel doped 1-D lithium titanate nanofibers ($Li_4Ti_5-xNi_xO_{12}$, where x=0, 0.05 and 0.1) have been successfully synthesized using a facile electrospinning process. Physical characterization reveals that nickel is homogeneously incorporated into the lattice of lithium titanate nanofibers (LTONF) which significantly improves their properties yielding outstanding electrochemical performance in a lithium ion battery at high rate rates and significant reduction in the voltage gap between the oxidation and reduction peaks. A capacity of 190 mA h g^{-1} has been obtained at 0.2 C for the 10% nickel doped nanofibers (Ni-LTONF$_{10}$), which is higher than the theoretical capacity of pristine lithium titanate (175 mA h g-1) and also shows superior rate capability resulting in 63 mA h g^{-1} obtained at 50 C, which is 20 times higher than that of un-doped pristine LTONF and lithium titanate nanoparticles (LTONP). Lastly, a hybrid supercapacitor is fabricated using Ni-LTONF$_{10}$, showing superior energy density at high power density.

Introduction

The developments of portable electronics, electric vehicles, and smart grids are increasing the need for reliable energy storage devices with safe operation and high power capabilities.[1, 2] Lithium ion batteries (LIBs) have been studied extensively in the past years as one of the most promising candidates for these applications. However, the current graphite-based electrode technologies used in LIBs suffer from limited power capabilities and safety concerns.[3] To address these challenges, researchers have investigated a number of alternative materials. Spinel lithium titanate (LTO) is one such material that is chosen for its safety, high power density, and rate capability which stem from its outstanding ability to accommodate lithium ions without significant structural change during charge and discharge operations (zero-strain).[4, 5] The theoretical capacity of LTO is 175 mA h g^{-1} with a stable plateau at 1.55 V versus Li/Li$^+$. This relatively high voltage minimizes the chance of lithium dendrite formation and electrolyte decomposition which usually occur at lower voltages, causing cell failure and possibly fire due to cell overheating. Although LTO has remarkable characteristics, its electrochemical performance and practical applications are still limited due to its poor electron conductivity and low

energy density.[6] Different approaches have been investigated to overcome these limitations such as carbon coating, particle size reduction, and transition metal doping.[3, 4] Carbon coating improves conductivity and rate capability of LTO, while particle size reduction shortens the lithium diffusion path which improves intercalation kinetics and improves battery capacity.[4] Doping with transition metals has been found to enhance conductivity and lithium ion diffusivity leading to higher capacity and improved rate capability.[7] Researches in metal doping have been focused mainly on lithium titanate nanoparticles (LTONP), nanowires, and nanotubes. [8-16]

Nickel is a highly abundant and inexpensive dopant that has the potential to improve the performance of LTO-based LIBs. Investigations on nickel doped LTO nanoparticles were conducted in the past. In some studies, nickel doped LTO nanoparticles were found to increase the initial capacity of the battery.[17, 18] Other studies found marginal improvement in the rate capability performance of nickel doped LTO nanoparticles synthesized using different methods, including hydrothermal and solid state reaction.[5, 19] Co-doping LTO with nickel and manganese was reported to improve capacity and cycling performance.[20] These investigations led to the development of advanced LTO materials. However, their improvements were incremental and no remarkable combined advancements in both rate capability and energy density have been reported yet.

On the other hand, 1D nanofibers are very attractive because they can be easily produced by low cost and facile

Chemical Engineering Department, University of Waterloo, 200 University Ave.
Waterloo Ontario, N2L 3G1, Canada
† E-mail: zhwchen@uwaterloo.ca

electrospinning, which makes the electrospun nanofibers highly scalable for large batch production. The principle of electrospinning is based on applying high voltage between an injected solution droplet and an opposing collector. Charge accumulation on the droplet surface causes electrostatic repulsion with the surface tension force which stretches the droplet to form what is known as Taylor cone.[21] When the applied voltage reaches critical value, the force of the electric field overcomes the surface tension force and the fiber jet elongates and is deposited on the collector. Electrospinning is affected by a number of parameters, including the solution viscosity and concentration, applied voltage, flow rate, solution conductivity, and the distance between the needle tip and the collector. The main advantages of electrospinning are the low cost, scalability, simplicity of the experimental setup, the high surface area and small pore size of the fibers that can be synthesized. The main disadvantages of electrospinning are the difficulty in obtaining uniform thickness of the fibers, fiber disruption, and the formation of large beads.[22, 23] In this work, we used sufficiently viscous PVP precursor solution and optimized the experiment parameters as explained in the experimental section to overcome these disadvantages.[24]

The 1D nanofibers can be very good choice for LIBs applications because 1D nanofibers show good strain relaxation, shorter Li$^+$ diffusion paths, interfacial control, and continuous electron transport pathways, which are all very favorable for improving LIB performance.[3, 25-28] Number of studies reported using 1D nanofibers in LIBs[29-31], however, nickel doped into LTO one-dimensional nanofibers has not yet been investigated and reported in literature[32]. In this work, we report successful in-situ doping of nickel into 1D lithium titanate nanofibers (LTONF) using facile and scalable electrospinning technique followed by a heat treatment. We investigated three Ni to LTO molar ratios; 0%, 5% and 10%. It is worth mentioning that 15% doping ratio was not possible at similar electrospinning parameters as the other three doping ratios. This can be attributed to the effect of the additional nickel on the precursor solution conductivity and charge density at the surface of the injected solution droplet. Increasing the nickel amount increases the solution conductivity and charge density beyond the critical value, which hinders the creation of Taylor cone required to initiate the elongation of fiber jets.[33, 34]

Our strategy in this work reporting nikel doping to LTO nanofibers for the first time is based on dual improvements for both electronic conductivity and lithium diffusivity of LTO in order to simultaneously enhance rate capability as well as energy density of the LIB. The advantage of our approach is the simplicity and unique coupling of in-situ nickel doping distributed homogenously into the stable 1D LTO nanofibers lattice. The obtained promising results can open the door for more research in the use of nanofibers for LIB applications. A performance comparison of nickel doped LTO nanofibers with previous studies is shown in **Table S1** in supporting information.

The pure LTONF sample with x=0 is referred to as LTONF, the sample with x=0.05 is referred to as Ni-LTONF$_5$, and for x=0.1, the samples is referred to as Ni-LTONF$_{10}$. While LTO nanoparticles is referred to as LTONP

Results and discussion

Characterization

The XRD pattern of all samples are shown in **Figure 1a**, the results show that all patterns are almost identical. The sharp diffraction peaks located at 2θ = 18.6^o, 37°, 43°, 58°, and 63° correspond to (111), (311), (400), (511), (440), and (531) planes, respectively. These peaks represent single phase spinel LTO with the Fd3m space group (JCPDS card number 49-0207) which reveals that calcination at 780 ^{o}C in air obtains well crystallized LTO with no indication of impurities. The crystallization process has significant effects on LIB performance because crystallinity and material purity affects both lithiation kinetics and lithiation capacity. Studies have shown that the initial crystallinity of TiO_2 can have an effect on the crystallization and purity of $Li_4Ti_5O_{12}$.[35, 36] Amorphous materials tend to hinder lithiation because of its disordered structure, while crystalline materials allow more facile lithiation.[36] Although the precursor nanofibers used are structurally amorphous because of low temperature hydrolysis of titanium alkoxide naturally leads to the formation amorphous TiO_2. Heat treatment of amorphous TiO_2 will form a crystalline phase of TiO_2 and then undergo solid-state conversion to crystalline phase of $Li_4Ti_5O_{12}$ via lithiation by the lithium source.[35, 36] The similarity in XRD patterns of doped and pure samples also indicate that nickel doping has not obviously changed the crystal structure of LTONF. However, broader peaks are found in LTONF, Ni-LTONF$_5$, and Ni-LTONF$_{10}$ XRD patterns compared to the LTONP XRD pattern. This difference is attributed to the crystal refinement of the nanofibers samples resulting from a difference in synthesis method. To verify the doping effect of nickel, the specific peak corresponding to the (111) plane for LTONF and Ni-LTONF$_{10}$ is magnified and shown in **Figure 1b**. Ni-LTONF$_{10}$ shows a slight shift in the diffraction peak of (111) plane to a lower angle (2θ = 18.51^o) compared to the diffraction peak of pure LTONF (2θ = 18.6^o). This decrease indicates that the lattice parameter of Ni-LTONF$_{10}$ is slightly higher than that of pure LTONF. This is attributed to the size of nickel (0.69 Å) being slightly larger than titanium (0.60 Å).[10, 19, 37] The shift in the diffraction peak is additional evidence for the successful doping of nickel which can be also observed in the change of color of the end product. As seen in the inset of **Figure 1b**.
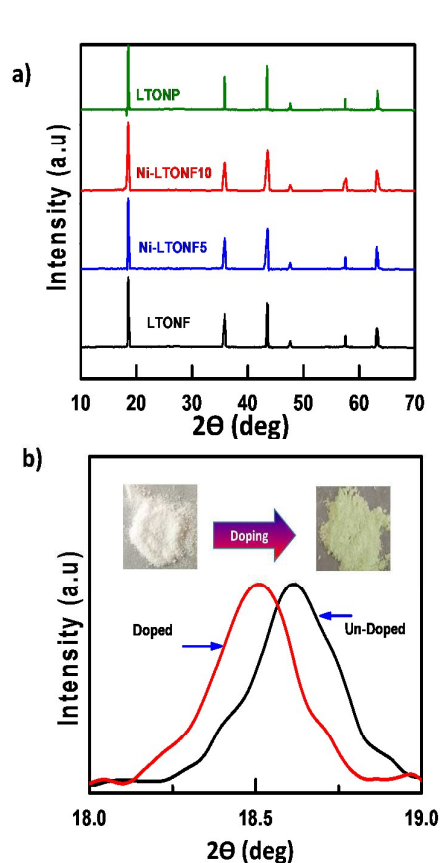
Figure 1.XRD patterns of LTONP, LTONF, Ni-LTONF5, and Ni-LTONF10 and, b) magnification of the XRD peak corresponding to the (111) plane of LTONF and Ni-LTONF10 showing a negative peak shift due to nickel doping. The inset shows optical images of LTO nanofibers before and after doping

The lattice parameters of the pure and doped LTO nanofibers are calculated by mathematical calculations using the following equations[38, 39]

$$2d (\sin\Theta) = n\lambda \qquad (1)$$

$$1/d^2 = (h^2+k^2+l^2)/a^2 \qquad (2)$$

Where d is the distance between the atomic layers, θ is the beam angle, n is integer number of wavelengths (1), λ is the wavelength of the incident beam. h, k, l are Miller indices and a is lattice parameter. The lattice parameters are found to be 8.366 Å, 8.373 Å and 8.379 Å for LTONF, Ni-LTONF$_5$ and, Ni-LTONF$_{10}$, respectively. The slight increase in the lattice parameter with increasing doping percentage is attributed to the slight expansion of the lattice due to the partial substitution of titanium with nickel which is also confirmed by XPS results
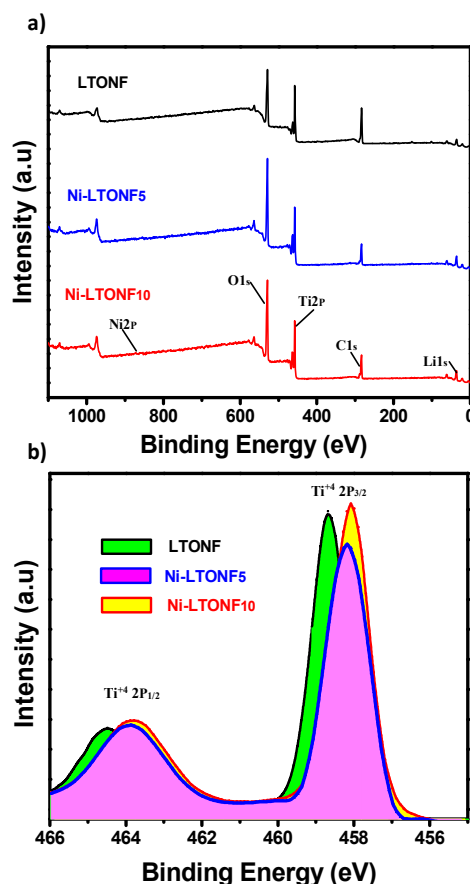

Figure 2.Figure 2. a) General XPS spectra of LTONF, Ni-LTONF5 and Ni-LTONF10 and, b) Magnification of XPS Ti2p peaks of LTONF, Ni-LTONF5 and Ni-LTONF10.

X-ray photoelectron spectroscopy (XPS) was utilized to investigate material composition before and after nickel doping of LTONF as shown in **Figure 2a** shows the general XPS spectra of three LTO nanofiber samples, while **Figure 2b** shows magnification of the XPS Ti2p peaks. The un-doped LTONF shows two peaks at 458.54 eV and 464.31 eV corresponding to the $2p_{1/2}$ and $2p_{3/2}$ peaks of Ti^{+4}. The peaks were shifted to a lower energy level after nickel doping with 458.21 eV and 463.91 eV for Ni-LTONF$_5$ and 458.07 eV and 463.82 eV for Ni-LTONF$_{10}$ which reveal the effect of nickel doping on changing the valence state of Ti ions from Ti^{+4} to Ti^{+3} leading to enhanced electrochemical properties as well documented in literature.[15, 40, 41]

The composition change of the LTO nanofibers before and after doping is summarized in **Table 1**. The results reveal that nickel doping causes the formation of Li$_4$Ti$_{(5-x)}$Ni$_x$O$_{12}$ (x=0.05 and 0.1) which explains the capacity increase of doped LTO at low current density compared to un-doped LTO.

Journal of Materials Chemistry A Accepted Manuscript

Table 1. Elemental composition (atomic percentage) of the LTO nanofibers samples

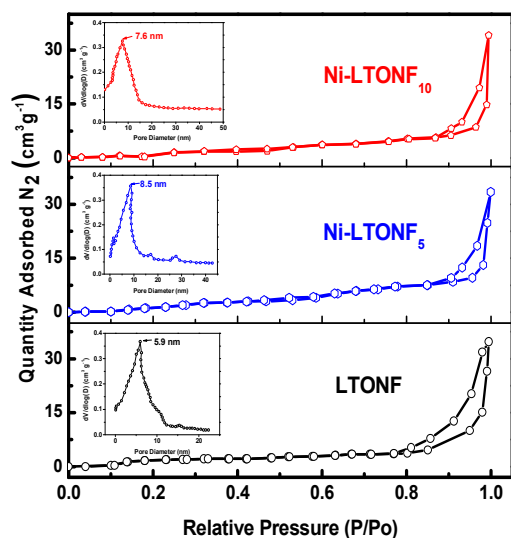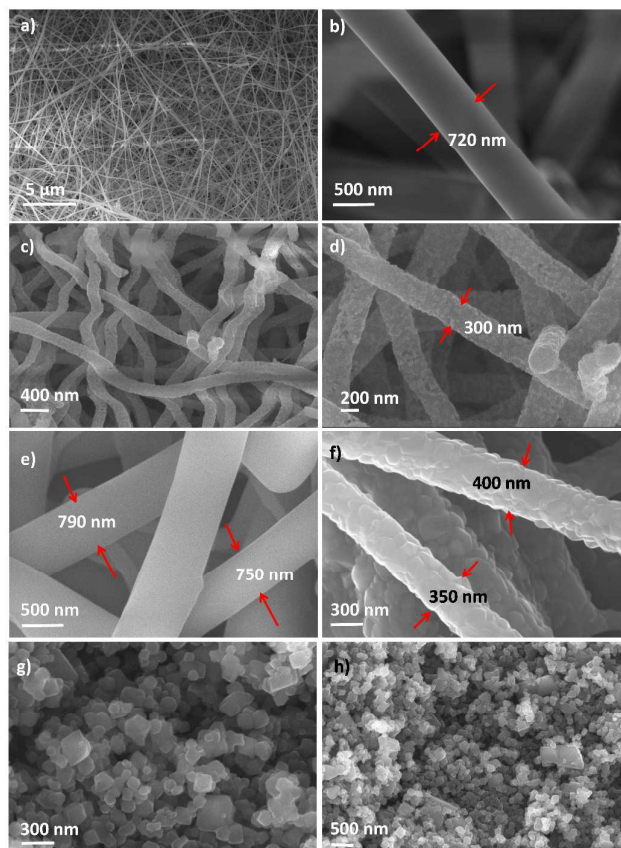|	LTONF	Ni-LTONF5	Ni-LTONF10
Lithium %	19.28	19.047	19.02
Titanium %	22.75	23.57	23.23
Oxygen %	57.97	57.14	57.06
Nickel %	0	0.24	0.49

Figure 3.Nitrogen adsorption/ desorption isotherm curves and the pore size distribution curves (inset)

The BET analysis of the three LTO nanofibers samples were measured. **Figure 3** shows the nitrogen adsorption/ desorption isotherm curves and the pore size distribution. The surface area for the three sample are found to be almost similar, with surface areas of 8.22 , 8.55 and, 7.96 m^2 g^{-1} for LTONF, Ni-LTONF$_5$, and Ni-LTONF$_{10}$, respectively. The average pore size diameter are found to be 5.9, 8.5 and 7.6 nm for LTONF, Ni-LTONF$_5$, and Ni-LTONF$_{10}$, respectively. The similarity in surface area and pore size are more indications that the improvement in electrochemical performance is mainly driven by nickel doping.

The SEM images of LTONF, Ni-LTONF$_{10}$ before and after calcination in addition to LTONP are shown in **Figure 4**. The nanofibers samples show continuous, fibrous morphology, with a diameter in the range of 700-800 nm before calcination and 300-400 nm after calcination. This reduction in diameter is due to the removal of PVP. The diameter of Ni-LTONF$_{10}$ is in the range of 750-850 nm before calcination which is reduced to 350-450 nm after calcination. The diameter of Ni-LTONF$_{10}$ before and after calcination maintained an average range of 50-100 nm difference in diameter compared to LTONF. Furthermore, both of the materials after calcination show homogeneous surface roughness, indicating that the granular-like structure of primary nanoparticles of LTONF maintains a fiber-like structure. This 1D nanofiber structure obtained after

calcination at 780°C is suitable for excellent lithium ion diffusion and electrical conductivity as demonstrated by significantly enhanced LIB performance shown later. The SEM images of LTONP confirm the nanoparticles morphology with a particle size range of 100-250 nm.

Figure 4. a-b) SEM image of electrospun LTONF before heat treatment at low and high magnifications, c-d) SEM images of the LTONF after heat treatment at low and high magnifications, e-f) high magnification SEM images of Ni-LTONF10 before and after heat treatment and, g-h) SEM images of LTONP after heat treatment

The TEM image of Ni-LTONF$_{10}$ in **Figure 5a** show the 1D morphology with aligned multigrain of nanoparticles. The lattice fringe fingerprint of HRTEM shown in **Figure 5b** indicates that the crystalline structure of Ni-LTONF$_{10}$ with a preferential orientation to plane (111). The polycrystalline structure of the material is revealed in the SAED pattern shown in **Figure 5c**. The EDS images shown in **Figure 5(d-g)** are based on high angle annular dark-field scanning transmission electron microscopy (HAADF-STEM) of one nanofiber. Combined with EDS line scan analysis shown in **Figure 5h** with the corresponding elemental distribution. Elemental characterization clearly confirms the homogenous distribution of nickel into the lattice of LTO. Electron energy loss spectroscopy (EELS) is a technique that shows atomic resolution of the elemental composition. The EELS mapping for part of the wire in **Figure 5d** is shown in **Figure 5(i-k)**, further

confirming the uniform distribution of nickel into the lattice of LTO (each pixel in these figures is equivalent to 6 nm x 6 nm).
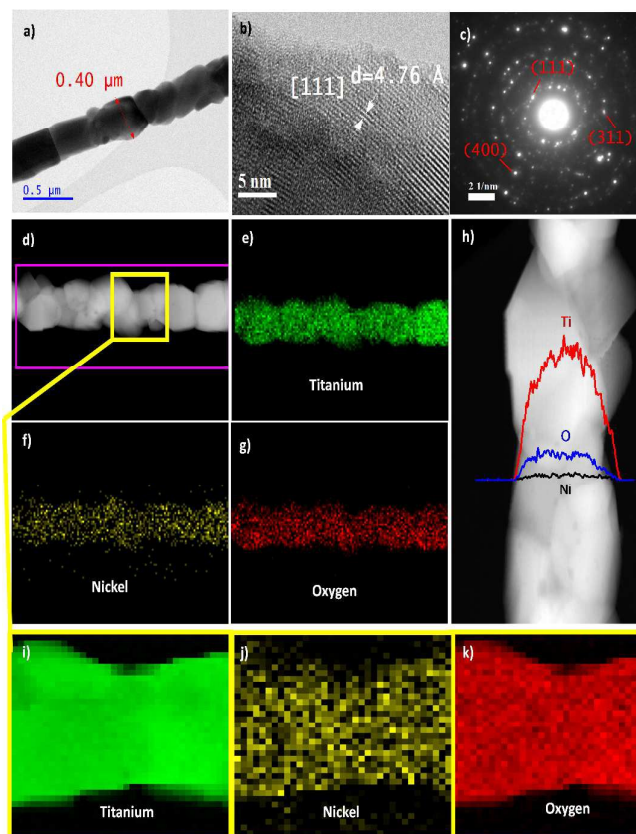

Figure 5.a) TEM images of Ni-LTONF10, b) high resolution TEM image of Ni-LTONF10, c) selected area electron diffraction pattern of Ni-LTONF10, d) HAADF-STEM image of Ni-LTONF10, e-g) EDS mapping of the nanofiber in (d) showing the elements titanium, nickel and oxygen, respectively, h) EDS line scan showing the elements profile across Ni-LTONF10, i-k) electron energy loss spectroscopy mapping of the labelled part in (d) showing the elements titanium, nickel and oxygen, respectively

Figure 6.a) Galvanostatic charge-discharge profiles of LTONP, LTONF, Ni-LTONF5, and Ni-LTONF10. d) Cyclic voltammetry showing changes in redox behavior of the LTO nanofiber materials with increase in nickel doping

Electrochemical performance

The LIB low current density charge-discharge tests were evaluated in potential range of (1- 2.5) V at room temperature using 0.2 C rate as shown in **Figure 6a**. LTONP has an energy capacity of 129 mA h g^{-1} while pure LTONF shows 149 mA h g^{-1} reversible capacity. Ni-LTONF$_5$ shows a higher capacity of 164 mA h g^{-1} while Ni-LTONF$_{10}$ shows excellent improvement with 190 mA h g^{-1} reversible capacity which is not only higher than LTONP, LTONF, and Ni-LTONF$_5$, but also higher than the theoretical capacity of LTO (175 mA h g^{-1}). **Figure 6b** shows the cyclic voltammetry test which was done in a voltage window of (1-2.5) V and scan rate of 0.5 mV s^{-1} for the 1D LTO electrospun samples to identify the change in redox behavior due to nickel doping. LTO is known to have a reduction peak at around 1.4 V and oxidation peak around at 1.7 V. The experimental results of LTONF show reduction and oxidation peaks similar to the standard LTO peaks indicating high crystallinity of the prepared sample.
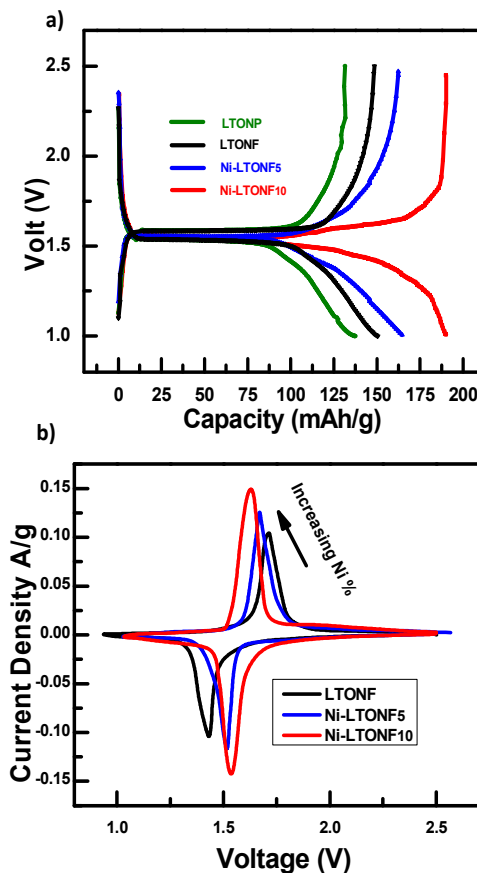
Increasing nickel doping causes changes in the redox behavior of the tested materials. The oxidation peaks of the three materials are located at 1.71 V, 1.67 V, and 1.625 V and the reduction peaks are located at 1.43 V, 1.53 V, and 1.52 V for the LTONF, Ni-LTONF$_5$, and Ni-LTONF$_{10}$, respectively. **Table 2** shows the voltage hysteresis (ΔV) between the reduction and oxidation peaks of the three samples. Ni-LTONF$_5$ shows 50% reduction in ΔV compared to LTONF while Ni-LTONF$_{10}$ shows outstanding reduction in voltage hysteresis with a value three times smaller than LTONF and sharper redox peaks. These changes indicate improved lithium diffusion kinetics due to the significant reduction in electrode polarization which allows for much faster rate in lithium uptake and release.[18, 42, 43]

Table 2. The oxidation and reduction peaks of the three samples with the voltage calculated hyteresis

	Oxidation	Reduction	ΔV
LTONF	1.71	1.43	0.29
LTONF$_5$	1.67	1.53	0.14
LTONF$_{10}$	1.62	1.52	0.1

Figure 7 shows the rate capability tests of LTONP, LTONF, Ni-LTONF$_5$ and Ni-LTONF$_{10}$ evaluated in potential range of (1- 2.5) V at room temperature using different current densities. The capacity fading for LTONP was very fast with increasing the C rates, showing only 25 mA h g^{-1} at 5 C only and below 5 mA h g^{-1} at 20 C, the capacity approached zero at C rates higher than 20 C. LTONF also suffered from fast capacity fading as LTONP but with better performance of 48 mA h g^{-1} at 20 C and below 5 mA h g^{-1} at 50. Ni-LTONF$_5$ showed improved performance compared to LTONP and LTONF with 81 mA h g^{-1} at 20 C and 38 mA h g^{-1} at 50 C**.** Lastly, Ni-LTONF$_{10}$ showed outstanding rate capability performance at high C rates with 116 mA h g^{-1} at 20 C and 63 mA h g^{-1} at 50 C.
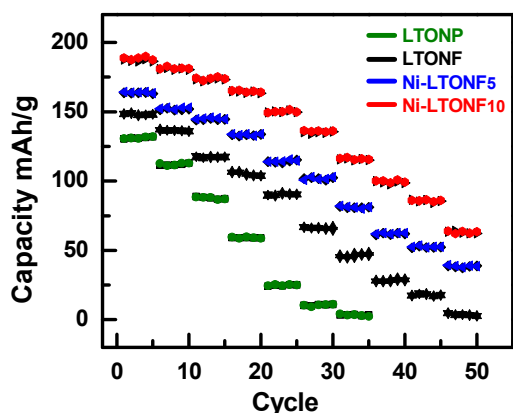

Figure 7. Rate capability of LTONP, LTONF, Ni-LTONF5 and Ni-LTONF10 measured at different current densities

A comparison between the performance of LTONF and Ni-LTONF$_{10}$ at low and high C rates is shown in **Figure 8a**. The result shows that the performance of Ni-LTONF$_{10}$ at 50 C is 20 times higher than LTONF. **Figure 8b** shows a comparison of the discharge capacity values of the 1D nanofiber LTO materials at different C rates as function of their discharge capacities at 0.2 C. The results prove that Ni-LTONF$_{10}$ maintains higher values at all C rates.

For further investigation on the effect of nickel doping on the durability and cycling behavior of the 1D nanofiber materials, the long cycling performance was evaluated at 10 C as shown in **Figure 8c**. LTONF maintains a discharge capacity of 57 mA h g^{-1} after 1000 cycles which corresponds to 85 % of the first discharge capacity (67 mA h g^{-1}). Ni-LTONF$_5$ maintains 90.6 mA h g^{-1} discharge capacity, corresponding a capacity retention of 89% (101.8 mA h g^{-1}). Ni-LTONF$_{10}$ shows the highest performance after 1000 cycles with 126.8 mA h g^{-1} discharge capacity corresponding to a capacity retention of 94% (134.9 mA h g^{-1}) and an average capacity loss per cycle equivalent to 8.09 x 10^{-3} mA h g^{-1}.
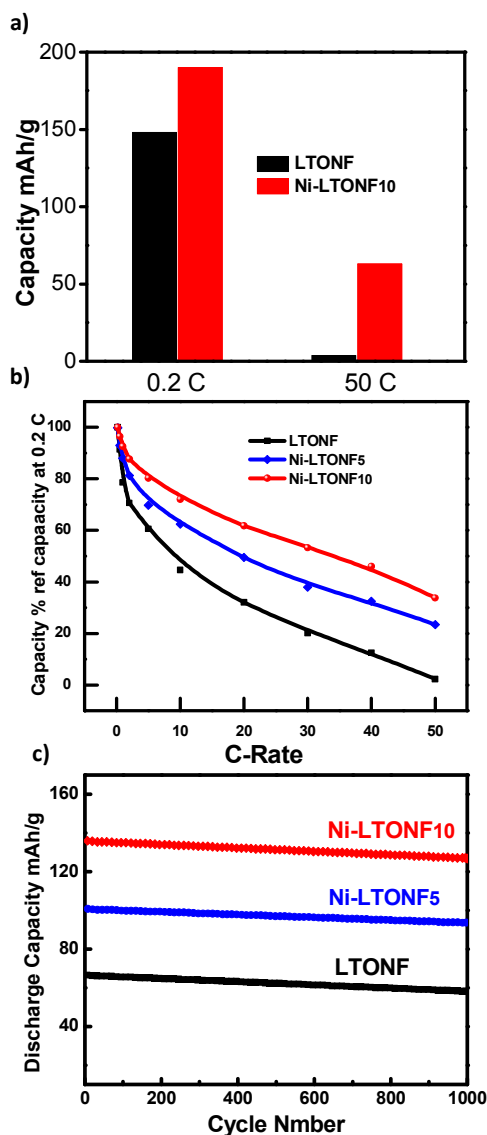

Figure 8.a) The performance of LTONF and Ni-LTONF10 at 0.2 C and 50 C showing the significant improvement of nickel doping at high C rates. b) Rate performance of LTONF, Ni-LTONF5, and Ni-LTONF10 at different C rates normalized to capacity at 0.2 C. c) Long term (1000 cycles) of LTONF, Ni-LTONF$_5$, and Ni-LTONF$_{10}$ at 10 C current density.

2D Raman mapping was utilized to investigate the stability of the 1D nanofibers morphology of un-doped LTONF and Ni-LTONF$_{10}$ before and after long cycling at high power rate (10 C). **Figure 9(a-b)** show the un-doped nanofibers before cycling at the electrode surface and at 10 μm depth, respectively, while **Figure 9(c-d)** show the un-doped nanofibers at the surface and at 10 μm depth after long cycling. **Figure 9(e-f)** show Ni-LTONF$_{10}$ nanofibers before cycling at the electrode surface and at 10 μm depth. **Figure 9(g-h)** show Ni-LTONF$_{10}$ nanofibers at the surface and at 10 μm depth after long cycling. The results show that 1D longitudinal nanofiber morphology was not damaged after long cycling for both

Journal of Materials Chemistry A Accepted Manuscript

doped and un-doped samples. The stable morphology of both electrode materials after long cycling at the surface and at the deepest point of the electrode indicates that the difference in the ability to maintain improved electrochemical performance between doped and un-doped samples is not attributed to morphological change or electrode deterioration of LTONF from long cycling at 10 C but rather to the effect of nickel in enhancing lithium intercalation thermodynamics for $LTONF_{10}$.
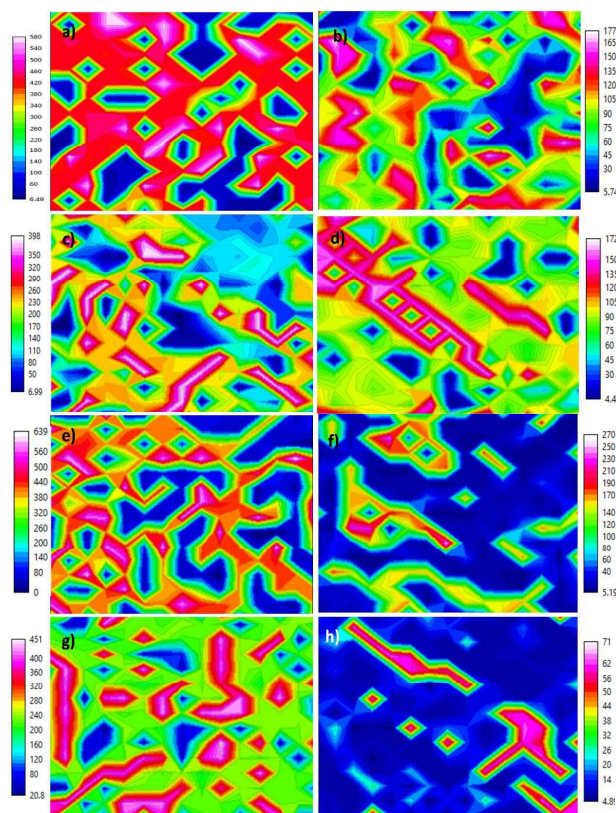

Figure 9.2D Raman mapping for LTONF and Ni-LTONF10 electrode, a-b) LTONF before cycling at the surface and at 10 μm, respectively, c-d) LTONF after cycling at the surface and 10 μm, respectively, e-f) Ni-$LTONF_{10}$ before cycling at the surface and at 10 μm, respectively and, g-h) Ni-$LTONF_{10}$ after cycling at the surface and at 10 μm, respectively

Electrochemical impedance spectroscopy (EIS) was employed to understand the effect of nickel doping on the lithium diffusivity and electrical conductivity. **Figure 10a** shows Nyquist plot of the impedance spectra for the three LTO nanofiber materials. All plots have a semicircle in the high frequency region and straight line in the low frequency zone. The low frequency zone is attributed to the diffusion of the lithium ions into the bulk of the electrode. **Figure 10b** shows the relationship between real impedance and the reciprocal square root of the lower angular frequencies $\omega^{-0.5}$. Lithium diffusion coefficients are calculated based on the following equations [44, 45]

$$Z_{re} = R_s + R_{ct} + \sigma_w \cdot \omega^{-0.5} \qquad (3)$$

$$D = 0.5(RT/An^2F^2 \sigma_w C)^2 \qquad (4)$$

Where R_s is the electrolyte resistance, R_{ct} is the charge transfer resistance at the surface of the active material, σ_w is Warburg impedance coefficient (Ω s$^{-0.5}$), ω is the angular frequency in the low frequency region ($\omega = 2\pi f$), D is the diffusion coefficient, R is the gas constant, T is the absolute temperature, F is Faraday's constant, A is the area of the electrode surface, and C is the molar concentration of Li$^+$ ions in 1 cm^3.
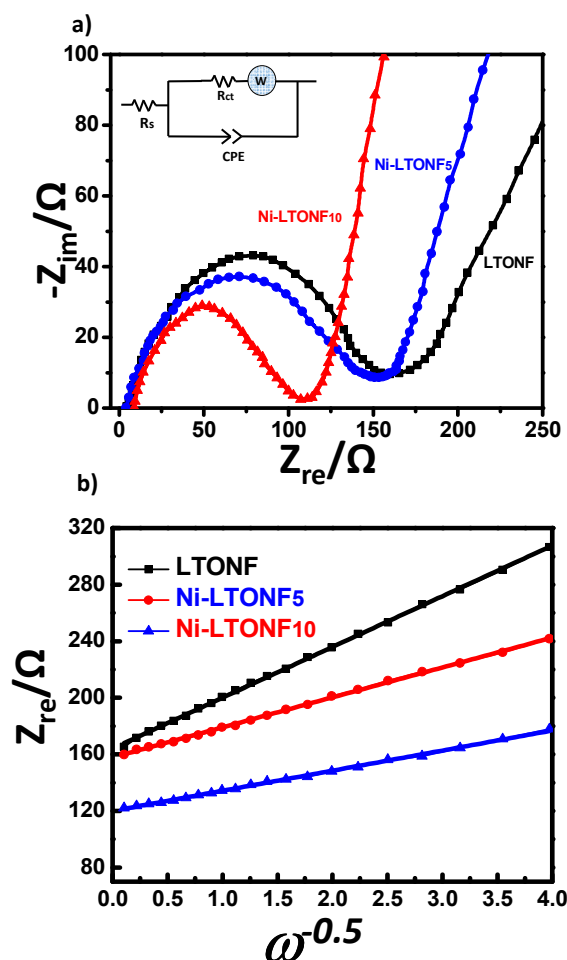
Figure 10. a) Nyquist plots of LTONF, Ni-LTONF5 and Ni-LTONF10 measured before cycling with the equivalent circuit shown in the inset, and b) the relationship between real impedance and $\omega^{-0.5}$.

Table 3 shows a summary of the calculated values of R_s, R_{ct}, σ_w and D. Ni-$LTONF_{10}$ shows 5.86 x 10^{-12} cm^2 s^{-1} which is significantly higher (17 times) than that of pure LTO (3.43 x 10^{-13} cm^2 s^{-1}). The results clearly show the effect of nickel doping on improving the lithium diffusion coefficient and enhancing the overall electrochemical performance of the LTO nanofibers.[45]

Table 3. EIS parameters of the three LTO nanofiber samples

	LTONF	Ni-LTONF5	Ni-LTONF10
Rs (Ω)	4.26	4.18	5.317
Rct (Ω)	160.1	153.08	114.29
σw (ΩS$^{-0.5}$)	35.91	21.2	14.22
D (cm^2/S)	3.43 X 10^{-13}	9.67 X 10^{-13}	5.86 X 10^{-12}

For further investigation, we fabricated an asymmetric hybrid supercapacitor (HSC) cell made of Ni-LTONF$_{10}$ material as the anode and commercial activated carbon (AC) as the cathode. The mass of ratio of the Ni-LTONF$_{10}$ to AC was 1:3 to balance the kinetics of the non-faradic and faradic components of HSC as described in the below equations:

$$AC + PF^6 \longleftrightarrow AC^+.PF^- + e^- \qquad (5)$$

$$Li_4Ti_5O_{12} + 3Li^+ + 3e^- \longleftrightarrow Li_4Ti_5O_{12} \qquad (6)$$

Figure 11a shows the charge/discharge profiles of HSC in voltage window (0–3) V measured at different current densities. All the curves show change in the voltage charge/discharge rates with gradual slope between 2 V and 3 V and sharper slope below 2V which is attributed to the difference in charge/discharge kinetics between battery portion of the HSC and the electrical double layer capacitor (EDLC) portion. The faradic Li$^+$ intercalation /de-intercalation reaction at the anode side happens concurrently with PF$_6$ double layer creation at the surface of both electrodes, causing gradual slop in the region (2 – 3) V.

Figure 11b shows the Ragone plot obtained from the discharge data in the voltage profile of the HSC measurement shown in **Figure 11a** at different current densities using the following equations[46, 47]:

$$E = 0.5 \, C \, \Delta V^2 \qquad (7)$$

$$P = E/dt \qquad (8)$$

$$C = I.dt \, /m.\Delta V \qquad (9)$$

where E is the energy density, C is the cell capacitance, ΔV is the potential window, P is the power density, dt is the discharge time and m is the total mass of active materials in both anode and cathode

The results clearly show that the hybridized supercapacitor has improved energy density at high power rates due to the additional faradaic reactions, improved conductivity and stability of 1D Ni-LTONF$_{10}$ anode material
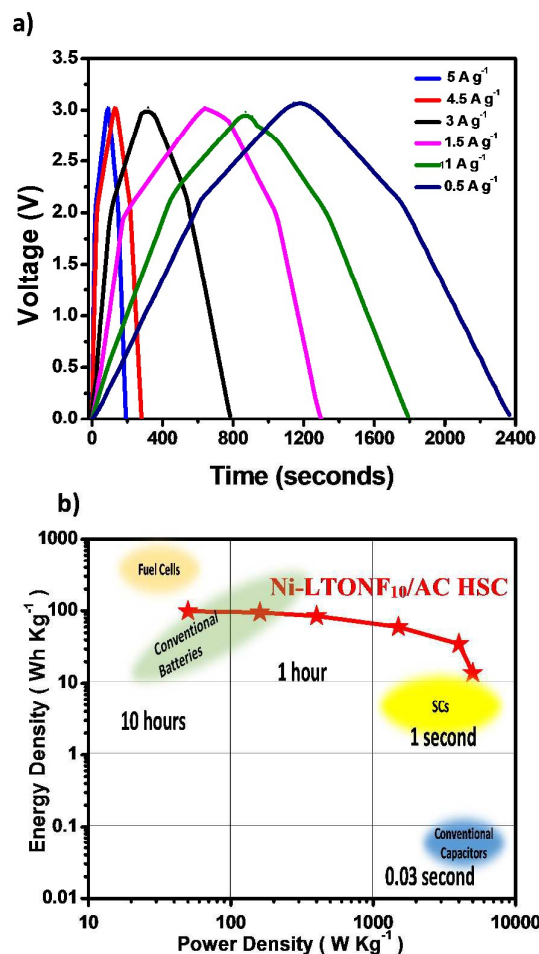

Figure 11. a) Charge/discharge profiles of HSC in voltage window (0-3) V measured at different current densities and, b) Ragone plot obtained from the discharge part in the voltage profile of HSC measurement at different current densities shown in Figure 11a

The explanation of all the improvements in electrochemical results shown in the previous results for the nickel doped LTO nanofibers material are attributed to the compositional change that happen to the LTO nanofibers due to the insertion of nickel into its lattice without noticeable effect on its structure in the formation of Li$_4$Ti$_{5-x}$Ni$_x$O$_{12}$ (x=0, 0.05 and 0.1). LTO has Fd3m space group with the 8a tetrahedral sites occupied by lithium ions, 16d octahedral sites shared between lithium ions and titanium ions (Ti^{+4}) with 1:5 ratio of lithium ions to titanium ions and 32e sites are occupied by oxygen[3, 4]. The octahedral 16c sites and the tetrahedral 8b and 48f sites are vacant which simplifies the intercalation and de-intercalation of lithium ions into the structure of LTO. This process accommodate up to three lithium ions as per equation (6) shown above. The transfer of lithium ion causes the phase of LTO to change from spinel (Li$_4$Ti$_5$O$_{12}$) to rock-salt phase (Li$_7$Ti$_5$O$_{12}$). Three lithium atoms at the 8a sites move during discharge to 16c sites and the inserted lithium ions occupy the vacant sites, this process is reversed during charge operation.

The lithium ion diffusivity of spinel phase is higher than rock-slat phase because of the full occupancy of lithium sites in rock-salt phase while the electronic conductivity of rock-salt phase is higher because the Ti oxidation state in spinel-phase is (+4) which limits its electronic conductivity while the average oxidation state of Ti in rock-salt phase is (+3.4) due to the existence of both Ti^{+3} (60%) and Ti^{+4} (40%).[48]

The nickel insertion and the formation of $Li_4Ti_{5-x}Ni_xO_{12}$ (x=0.05 and 0.1) and the change in the valence state of Ti ions from Ti^{+4} to Ti^{+3} confirmed by XPS results have positively affected the lithium transfer process and enhanced the efficiency with which LTO is utilized for Li^+ storage by making the entire LTO material accessible for intercalation leading to higher initial capacity. The dual improvement in electronic conductivity due to nickel doping and improved lithium diffusivity in well crystalized 1D nanofiber morphology with good strain relaxation, shorter distance for Li^+ diffusion, interfacial control, continuous electron transport pathways and structure stability[49, 50] further improved the thermodynamics of lithium intercalation reactions because nickel is well distributed across all the LTO structure as shown in the TEM image which not only enhanced and accelerated the intercalation/de-intercalation process of Li^+ ion, but also helped LTO to maintain fast lithium ion diffusion kinetics at high current rates leading to excellent capacity at high power rates as LIB anode material and outstanding energy densities at high power densities in asymmetric hybrid super capacitor. The improved results of Ni-LTONF$_{10}$ compared LTONF$_5$ to can be attributed to the additional amount of nickel which further improved the LTO initial capacity and lithium intercalation thermodynamics

Materials

All materials were purchased from Sigma Aldrich and used without further purifications.
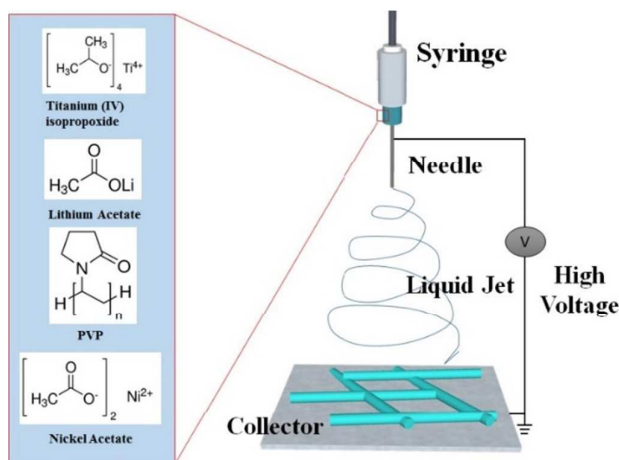
Experimental setup

Figure 12.Electrospinning experimental setup

Electrospinning technique shown in **Figure 12** has been utilized to produce nickel doped 1-D lithium titanate nanofibers ($Li_4Ti_{5-x}Ni_xO_{12}$) using titanium(IV) isopropoxide, lithium acetate, nickel acetate and poly-vinylpyrrolidone (PVP) as the precursors

Synthesis of LTO Nanofibers

0.95 g titanium(IV) isopropoxide ($Ti[OCH(CH_3)_2]_4$), 0.1855 g lithium acetate dihydrate ($LiC_2H_3O_2\cdot2H_2O$), and 0.51 g poly-vinylpyrrolidone (PVP, MW=1.3 M) were all added to a vial containing 8.5 ml pure ethanol and 2.5 ml acetic acid. The solution was stirred for 6 hours on a hot plat at 35^oC and 1150 rpm. The precursor solution was then moved to a 14.1 mm plastic syringe with metallic needle attached to a high voltage source (19.0 kV). The needle tip was placed 14.5 cm from an aluminum foil current collector and the flow rate was set to 0.15 ml h^{-1}. The collected fibers were moved to a quartz tube and annealed inside a tubular furnace at 780^oC in air for 5 hours (3^oC min^{-1}) to remove all organic materials. Finally, the sample was left to cool naturally before collecting the end product

Synthesis of Ni-LTO Nanofibers

Nickel doped LTO nanofibers were synthesized by adding (drop wise) a proper amount of nickel acetate solution dissolved in 2 ml ethanol to the precursor solution described in the LTONF synthesis. The rest of steps followed the same procedure as LTONF synthesis. The investigated materials include pure LTO nanofibers (LTONF) and two nickel to LTO mole ratios (1:20 and 1:10)

Synthesis of LTO Nanoparticles

LTO nanoparticles were synthesized by combining stoichiometric amounts of lithium carbonate (Li_2CO_3) and titanium dioxide (TiO_2) in a planetary ball mill using a 125 ml grinding jar and zirconium balls. The material was ball milled for 12 hours under 300 RPM. The resulting fine powder was then heat-treated at 780^oC at air to produce LTO nanoparticles

Morphology and structure Characterization

The crystal structure of the samples were characterized by X-ray diffraction (XRD, RIETVELDXRG 3000) and X-ray photoelectron spectroscopy (XPS, PHI Quantera) located at the Ontario Center for Characterization of Advanced Materials (University of Toronto). BET analysis was performed after samples were degassed at 200^oC for two hours under vacum. 2D raman mapping was examined using Senterra 2 Bruker Raman instrument. Sample morphology was examined using scanning electron microscopy (SEM, ZEISS ULTRA PLUS), Raman spectroscopy (SENTERRA 314) and transmission electron microscopy (TEM, JEOL 2010F TEM/STEM field emission microscope) at the Canadian center for electron microscopy (CCEM) located at McMaster University

Cell Fabrication

The electrochemical tests of LIBs were conducted by fabricating the electrode materials into coin cells. Each coin cell was made of a working electrode, seperator and lithium foil electrode in an organic electrolyte medium. The working electrodes was prepared by mixing the synthesized material with carbon black (super P) using a mortar and pestle for 30 minutes. Polyvinylidene fluoride (PVDF) binder was then added, and the mixture ground again for 20 minutes. The ratio of synthesized material, super P, and PVDF was 80:10:10. N-methyl-pyrrolidone (NMP) solvent was added to make a slurry which was coated on a 1 cm^2 copper current collector. The loading for all electrodes was approximately 1.0 mg cm^{-2}. The coated electrodes were dried at 80^oC for 2 hours followed by overnight drying in a vacuum oven at 110^oC in order to remove all the NMP solvent.

The HSC cells were fabricated from Ni-LTONF$_{10}$ material as the anode, seperator and commercial activated carbon (AC) as the cathode. The anodic electrode of HSC was prepared using 80 wt% active material, 10 wt% carbon black, and 10 wt% PVDF binder.

Coin cells for both LIBs and HSC were assembled in a glove box filled with argon. 1M lithium hexafluorophosphate (LiPF$_6$) in ethylene carbonate and dimethyl carbonate (EC-DMC 1:1 volume) was used as the electrolyte

Conclusion

As a conclusion, dual improvement of LTO properties was done through in-situ nickel doping to 1D lithium titanate nanofibers synthesized by facile electrospinning technique. The nickel insertion changed the chemical composition of LTO nanofibers without affecting the spinel crystal structure. The doped LTO nanofibers show improved capacity and outstanding rate capability at high power rates. The 10% nickel doped LTO nanofibers material showed initial capacity of 190 mAh g^{-1} and 63 mAh g^{-1} at 50 C with smaller voltage gap between the oxidation and reduction peaks compared to LTONF and Ni-LTONF$_5$. The hybridization of the 10% doped material into asymmetric supercapacitor also showed improved energy density at high power rates. Characterization techniques confirmed the homogenous distribution of nickel into the structure of LTO without affecting the crystal structure or noticeable effect on the LTO lattice size. The nanofibers longitudinally 1D morphology is obtained in both doped and un-doped LTONF with some increase in the nanofibers diameters in nickel doped LTONF. The characterization techniques also confirmed stable nanofiber morphology after long cycling

References

1. G.-N. Zhu, Y.-G. Wang and Y.-Y. Xia, *Energy & Environmental Science*, 2012, **5**, 6652-6667.
2. Z. Ding, L. Zhao, L. Suo, Y. Jiao, S. Meng, Y.-S. Hu, Z. Wang and L. Chen, *Physical Chemistry Chemical Physics*, 2011, **13**, 15127-15133.
3. T.-F. Yi, S.-Y. Yang and Y. Xie, *Journal of Materials Chemistry A*, 2015, **3**, 5750-5777.
4. X. Sun, P. V. Radovanovic and B. Cui, *New Journal of Chemistry*, 2014, **39**, 38-63.
5. B. Zhao, R. Ran, M. Liu and Z. Shao, *Materials Science and Engineering: R: Reports*, 2015, **98**, 1-71.
6. Y.-M. Jiang, K.-X. Wang, H.-J. Zhang, J.-F. Wang and J.-S. Chen, *Scientific Reports*, 2013, **3**, 3490.
7. T.-F. Yi, L.-J. Jiang, J. Shu, C.-B. Yue, R.-S. Zhu and H.-B. Qiao, *Journal of Physics and Chemistry of Solids*, 2010, **71**, 1236-1242.
8. J.-G. Kim, D. Shi, M.-S. Park, G. Jeong, Y.-U. Heo, M. Seo, Y.-J. Kim, J. Kim and S. Dou, *Nano Research*, 2013, **6**, 365-372.
9. B. Zhang, Z.-D. Huang, S. W. Oh and J.-K. Kim, *Journal of Power Sources*, 2011, **196**, 10692-10697.
10. X. Li, M. Qu, Y. Huai and Z. Yu, *Electrochimica Acta*, 2010, **55**, 2978-2982.
11. H. Wu, S. Chang, X. Liu, L. Yu, G. Wang, D. Cao, Y. Zhang, B. Yang and P. She, *Solid State Ionics*, 2013, **232**, 13-18.
12. H. Zhao, Y. Li, Z. Zhu, J. Lin, Z. Tian and R. Wang, *Electrochimica Acta*, 2008, **53**, 7079-7083.
13. S. Huang, Z. Wen, X. Zhu and Z. Lin, *Journal of Power Sources*, **165**, 408-412.
14. Y. K. Sun, D. J. Jung, Y. S. Lee and K. S. Nahm, *Journal of Power Sources*, 2004, **125**, 242-245.

15. H. Song, S.-W. Yun, H.-H. Chun, M.-G. Kim, K. Y. Chung, H. S. Kim, B.-W. Cho and Y.-T. Kim, *Energy & Environmental Science*, 2012, **5**, 9903-9913.

16. J.-G. Kim, M.-S. Park, S. M. Hwang, Y.-U. Heo, T. Liao, Z. Sun, J. H. Park, K. J. Kim, G. Jeong, Y.-J. Kim, J. H. Kim and S. X. Dou, *ChemSusChem*, 2014, **7**, 1451-1457.

17. Y.-J. Hao, Q.-Y. Lai, J.-Z. Lu and X.-Y. Ji, *Ionics*, 2007, **13**, 369-373.

18. J. Kim, S.-W. Kim, H. Gwon, W.-S. Yoon and K. Kang, *Electrochimica Acta*, 2009, **54**, 5914-5918.

19. C. Lin, M. O. Lai, L. Lu, H. Zhou and Y. Xin, *Journal of Power Sources*, 2013, **244**, 272-279.

20. W. Long, X. Wang, S. Yang, H. Shu, Q. Wu, Y. Bai and L. Bai, *Materials Chemistry and Physics*, 2011, **131**, 431-435.

21. M. S. Wilm and M. Mann, *International Journal of Mass Spectrometry and Ion Processes*, **136**, 167-180.

22. J. Wu, N. Wang, Y. Zhao and L. Jiang, *Journal of Materials Chemistry A*, 2013, **1**, 7290-7305.

23. B. Zhang, F. Kang, J.-M. Tarascon and J.-K. Kim, *Progress in Materials Science*, 2016, **76**, 319-380.

24. P. Gupta, C. Elkins, T. E. Long and G. L. Wilkes, *Polymer*, 2005, **46**, 4799-4810.

25. F. Wu, X. Li, Z. Wang and H. Guo, *Ceramics International*, 2014, **40**, 13195-13204.

26. J. Wolfenstine and J. L. Allen, *J. Power Sources*, 2008, **180**, 582-585.

27. L. Cheng, J. Yan, G.-N. Zhu, J.-Y. Luo, C.-X. Wang and Y.-Y. Xia, *Journal of Materials Chemistry*, 2010, **20**, 595-602.

28. M. R. Jo, Y. S. Jung and Y.-M. Kang, *Nanoscale*, 2012, **4**, 6870-6875.

29. V. Aravindan, J. Sundaramurthy, P. Suresh Kumar, Y.-S. Lee, S. Ramakrishna and S. Madhavi, *Chemical Communications*, 2015, **51**, 2225-2234.

30. H. Li, L. Shen, B. Ding, G. Pang, H. Dou and X. Zhang, *Nano Energy*, 2015, **13**, 18-27.

31. J. G. Kim, M. S. Park, S. M. Hwang, Y. U. Heo, T. Liao, Z. Sun, J. H. Park, K. J. Kim, G. Jeong, Y. J. Kim, J. H. Kim and S. X. Dou, *ChemSusChem*, **7**, 1451-1457.

32. J.-W. Jung, C.-L. Lee, S. Yu and I.-D. Kim, *Journal of Materials Chemistry A*, 2016, **4**, 703-750.

33. C. J. Angammana and S. H. Jayaram, *IEEE Transactions on Industry Applications*, 2011, **47**, 1109-1117.

34. A. Haider, S. Haider and I.-K. Kang, *Arabian Journal of Chemistry*, DOI: http://dx.doi.org/10.1016/j.arabjc.2015.11.015.

35. T. D. Tran, J. H. Feikert, X. Song and K. Kinoshita, *Journal of The Electrochemical Society*, 1995, **142**, 3297-3302.

36. Y. Shen, M. Søndergaard, M. Christensen, S. Birgisson and B. B. Iversen, *Chemistry of Materials*, 2014, **26**, 3679-3686.

37. K. Zaghib, M. Simoneau, M. Armand and M. Gauthier, *Journal of Power Sources*, 1999, **81–82**, 300-305.

38. Y.-R. Jhan and J.-G. Duh, *Electrochimica Acta*, 2012, **63**, 9-15.

39. D. Capsoni, M. Bini, V. Massarotti, P. Mustarelli, G. Chiodelli, C. B. Azzoni, M. C. Mozzati, L. Linati and S. Ferrari, *Chemistry of Materials*, 2008, **20**, 4291-4298.

40. D.-D. Han, G.-L. Pan, S. Liu and X.-P. Gao, *RSC Advances*, 2015, **5**, 92354-92360.

41. F. Li, M. Zeng, J. Li, X. Tong and H. Xu, *RSC Advances*, 2016, **6**, 26902-26907.

42. S. Huang, Z. Wen, Z. Gu and X. Zhu, *Electrochimica Acta*, **50**, 4057-4062.

43. S. Ganapathy, E. R. H. van Eck, A. P. M. Kentgens, F. M. Mulder and M. Wagemaker, *Chemistry – A European Journal*, **17**, 14811-14816.

44. Z. Yu, X. Zhang, G. Yang, J. Liu, J. Wang, R. Wang and J. Zhang, *Electrochimica Acta*, 2011, **56**, 8611-8617.

45. J. Jamnik and J. Maier, *Journal of the Electrochemical Society*, 1999, **146**, 4183-4188.

46.   T. Chen and L. Dai, *Journal of Materials Chemistry A*, 2014, **2**, 10756-10775.

47.   S. Roldán, D. Barreda, M. Granda, A. E. M. Á. S. R. MenéndezCurrent address: Cic Energigune, R. Santamaría and C. Blanco, *Physical Chemistry Chemical Physics*, 2014, **17**, 1084-1092.

48.   D. Liu, C. Ouyang, J. Shu, J. Jiang, Z. Wang and L. Chen, *physica status solidi (b)*, **243**, 1835-1841.

49.   C. K. Chan, H. Peng, G. Liu, K. McIlwrath, X. F. Zhang, R. A. Huggins and Y. Cui, *Nat Nano*, 2008, **3**, 31-35.

50.   L. Mai, Y. Dong, L. Xu and C. Han, *Nano Letters*, 2010, **10**, 4273-4278.

Journal of Materials Chemistry A Accepted Manuscript